

PET Systems

THOMAS LEWELLEN* and JOEL KARP†

*Department of Radiology, University of Washington Medical Center, Seattle, Washington

†Department of Radiology, University of Pennsylvania, Philadelphia, Pennsylvania

- I. Basic Positron Emission Tomography Principles
- II. Detector Designs
- III. Tomography System Geometry
- IV. Positron Emission Tomography Scintillators
- V. Positron Emission Tomography System Electronics
- VI. Attenuation Correction
- VII. Scatter Correction
- VIII. Noise Equivalent Count Rate
- IX. Future Trends

I. BASIC POSITRON EMISSION TOMOGRAPHY PRINCIPLES

The goal of positron emission tomography (PET) is to generate images of the distribution of positron emitters *in vivo*. PET systems rely on the detection of annihilation gamma rays that follow positron decay. The gamma rays are detected in coincidence by detectors that surround the patient. Figure 1 depicts a detector ring system with a diagram to illustrate the event rates from two detectors. Note that only a small number of the events processed by each detector are in coincidence. The rate of events processed by each detector is often referred to as the single event rate for that detector, whereas the coincidence event rate includes true events, scattered events, and random events. We discuss in more detail issues of scanner geometry and their effect on count rate in following sections.

The spatial resolution of PET imaging is limited by the fundamental nature of positron annihilation (Phelps *et al.*, 1975; Muehllehner *et al.*, 1976; Hoffman and Phelps, 1978; Derenzo, 1979). As positrons travel through human tissue, they give up their kinetic energy principally by Coulomb interactions with electrons. Because the rest mass of the positron is the same as that of the electron, the positrons may undergo large deviations in direction with each Coulomb interaction and they follow a tortuous path through the tissue as they give up their kinetic energy (see Fig. 2). When the positrons reach thermal energies, they interact with electrons by the formation of a hydrogen-like orbiting pair called positronium. Positronium is unstable and eventually decays, via annihilation, into a pair of anti-parallel 511-keV photons (emitted at 180° relative to one another). Note that a small percentage, less than 2%, annihilate without forming positronium. Although the radial distribution of annihilation events is sharply peaked at the origin (site of positron creation), a calculation of the radius that includes 75% of all annihilation events gives a realistic comparison of the impact of the maximum positron energy on the spatial resolution of PET imaging (Hoffman and Phelps, 1976). Table 1 lists the major emitters used in PET imaging, along with positron energy and range in water.

In addition to the positron range, the variation in the momentum of the positron also leads to a limitation of the spatial resolution of PET imaging. One would normally expect the annihilation gamma rays to be anti-parallel. However, the variation in momentum of the positron results in an

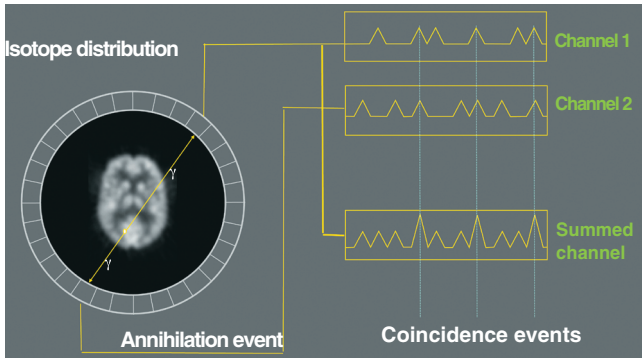


FIGURE 1 Block diagram of a basic PET scanner with illustration of events in coincidence.

TABLE 1 Half-life and positron range of isotopes commonly used in PET^a

Isotope	Half-Life (min)	Maximum Positron energy (MeV)	Positron Range in Water (mm)
¹¹ C	20.3	0.96	2.1
¹³ N	9.97	1.19	—
¹⁵ O	2.03	1.7	—
¹⁸ F	109.8	0.64	1.2
⁶⁸ Ga	67.8	1.89	5.4
⁸² Rb	1.26	3.15	12.4

^aThe range is defined as the radius that includes 75% of all annihilation events.

TABLE 2 Resolution Loss Due to Noncolinearity versus Tomograph Detector Ring Diameter^a

Ring Diameter, <i>D</i> (cm)	Resolution Loss, Δx (mm)
60	1.3
80	1.7
100	2.2

^aCalculated using the relationship $\Delta x = 0.5 D \tan 0.25^\circ$.

angular uncertainty in the direction of the 511-keV photons that is approximately 4 mrad (0.23°) (Beneditti *et al.*, 1950). This is referred to as noncolinearity. Table 2 shows the resolution loss due to noncolinearity as a function of detector ring diameter.

A third significant factor limiting PET image resolution is the intrinsic spatial resolution of the detector (Hoffman *et al.*, 1982). The resolution of a single detector is often quantified by the full width at half-maximum (FWHM) of the position spectrum obtained for a collimated point source placed before the detector at a fixed distance from it. The coincidence detector-pair resolution is normally specified as the FWHM of the point-spread function (PSF) obtained

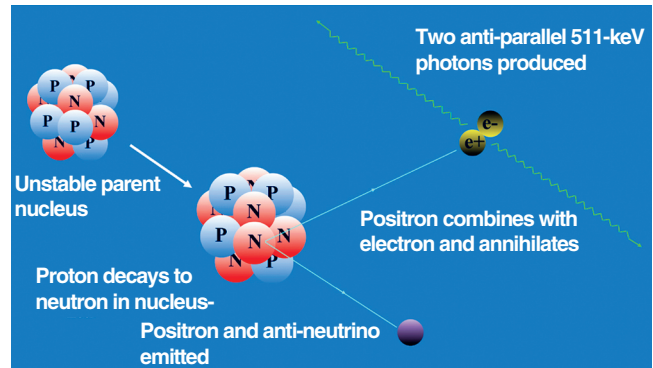


FIGURE 2 Physics of positron decay and annihilation, which results in two 511-keV gamma rays.

TABLE 3 Loss of System Spatial Resolution Due to the Combination of Positron Range and Gamma-Ray Noncolinearity for a 80-cm Ring Diameter and as a Function of Coincidence Detector Pair Resolution

Detector Pair Resolution (mm)	¹¹ C (mm)	⁶⁸ Ga (mm)	⁸² Rb (mm)
0	2.3	3.1	3.3
2	3.2	4.1	7.4
6	6.6	7.4	9.2

from the convolution of the two individual detector PSFs (Muehllehner *et al.*, 1986). For a detector composed of small discrete crystals, all interactions are assumed to occur at the center of individual crystals for the purpose of backprojection and image reconstruction. As a result, the PSF for such detectors is similar to a step function with a total width equal to the size of a crystal. The coincident PSF is, therefore, a triangular function whose base width is again equal to a crystal size. Thus, the FWHM of the coincident detector PSF is one-half the crystal size.

Together, the positron range, noncolinearity, and detector PSF limit the resolution of PET tomographs. Table 3 shows the impact of positron range on the detector-pair resolution for a 80-cm ring diameter (Nohara *et al.*, 1985). The resolution broadening effects due to positron range and noncolinearity for three isotopes (three different maximum positron energies) are tabulated for an infinitively small point source between two detectors for three coincidence detector-pair resolutions (0, 2, and 6 mm).

A final factor affecting PET image resolution is referred to as the parallax error, which results from the uncertainty of the depth of interaction (DOI) of the gamma rays in the crystal. Gamma rays travel some (unknown) distance in the crystal (or adjacent crystals) before being completely absorbed (see Fig. 3). As a result, if the gamma ray enters the crystal at an oblique angle, the location of the interaction will not be the same as the point of entry into the crystal;

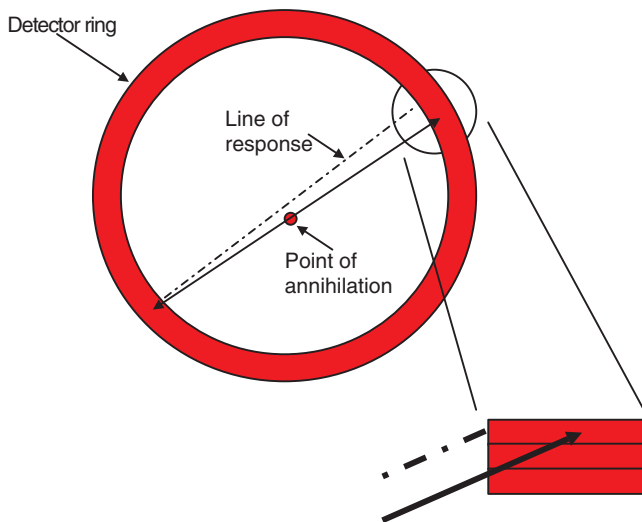


FIGURE 3 Parallax error. The gamma ray (solid line) interacts in a crystal after penetrating one or more adjacent crystals in the detector ring. Without depth-of-interaction information, the detection electronics will incorrectly assign the line of response (the dotted line) based on the front of the interaction crystal.

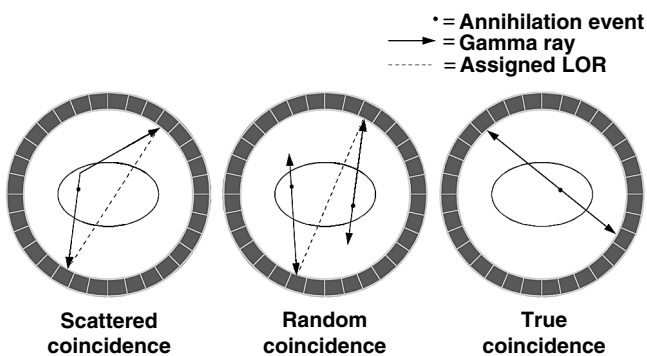


FIGURE 4 The three types of coincidence events measured in a PET scanner.

the crystal of the interaction may not even be the same as the one first entered. Thus, unless the DOI within a crystal can be accurately determined, an incorrect line of response (LOR) will be assigned to this interaction because the LOR is normally assigned to a position at the front of the crystal of interaction. The parallax effect worsens as the source position moves radially away from the center of the scanner because a larger fraction of the gamma rays enter the crystals at oblique angles.

Figure 4 illustrates three kinds of coincidence events that the tomograph accepts: (1) scattered events in which one or both gamma rays scatter within the patient; (2) random coincidences, in which two separate decays result in the detection of only one gamma ray from each one and the two events are close enough in time to be in coincidence; and (3) true coincidences, in which gamma rays are detected from a single decay that have not scattered in the patient. Our goal in PET imaging is to measure and reconstruct the distribution

TABLE 4 Options to Increase Detected Coincidence Events in a PET Study

Increase the patient dose
Use more efficient scintillators/detectors
Use more of the energy spectrum
Increase solid angle

of true coincidences while minimizing the scattered and random coincidences and correcting for the bias (but not necessarily the noise) associated with scattered and random coincidences. Note that both true and scattered events are referred to as prompt events because they come from the decay of a single nucleus and, thus, the gamma rays are detected almost simultaneously. Random, or accidental, coincidences occur if two separate decays occur close enough in time to look like a single decay to the system electronics. The prompt rate (trues + scatters) is related linearly to the activity in the patient. However, the randoms rate increases as the square of the activity in the patient and becomes more dominant at higher activity levels.

Increasing the number of true coincidences leads to less noise in the image and allows one to reconstruct the data with high spatial resolution of the distribution of decay events, given the physical limitations already discussed. Specific design goals are generally determined by the application (e.g., small animal imaging, human neurological scanning, or human whole-body imaging). But for any design goal, if the variance in the data is too high, then the reconstruction algorithm will have to employ a filter to reduce the image variance at the expense of spatial resolution (Phelps *et al.*, 1982). The four major options for improving counts per unit dose in a study are listed in Table 4.

Before looking at some of the consequences for detector and electronics design when we increase sensitivity, let us consider the basic options in Table 4. Many centers with dedicated PET scanners are already using the maximum dose limits allowed in their institutions (between 10 and 20 mCi for ^{18}F -FDG, fluoro deoxyglucose); increasing the patient dose is not a practical approach because higher doses would result in higher radiation exposures to the patient. This would only be advantageous for 2D systems because 3D volume-imaging PET systems (without interplane septa) generally reach the peak count-rate performance below 20 mCi due to random coincidence or because the detector and electronics become count-rate limited at high activity levels. In fact, 3D scanners consisting of large, continuous NaI(Tl) detectors use less than 10 mCi, due to count-rate limitations.

Many research facilities are searching for better scintillators, but materials with higher stopping power than bismuth germanate (BGO) have proved to be elusive. The main advantages of new scintillators (discussed in more detail later) such as lutetium oxyorthosilicate (LSO), in

comparison to BGO, is the combination of high light output and fast decay. BGO-based systems typically use detectors 30 mm deep, which provide approximately 90% detection efficiency for 511-keV gamma rays (therefore, 82% coincidence efficiency). Although 100% detection efficiency would improve sensitivity even further, no systems have yet been built with basic detection efficiency greater than that provided by 30-mm-deep BGO crystals.

One approach to gain more sensitivity is to use more of the energy spectrum—to accept events with energy less than the photopeak. This approach has been studied in dual-headed gamma cameras when they are operated as coincidence detectors because the sensitivity of the NaI(Tl) detectors is relatively low compared to those in dedicated PET scanners (Nelleman *et al.*, 1995). Two energy windows are set—one around the photopeak and one around a region of the Compton scatter spectrum. The lower window captures those events that Compton-scatter in the detector and then escape, producing events with energies in the Compton region of the spectrum. However, the inclusion of the Compton region also increases the amount of patient scatter, which also produces events with energies below the 511-keV photopeak. Although this technique can lead to an increase in sensitivity of close to a factor of 2, the increased scatter is problematic and, overall, the technique has not been shown to be clinically useful.

The fourth method to increase the solid angle is the most useful approach for dedicated PET systems. Techniques being developed include the removal of all axial collimation (3D volume imaging), reducing ring diameters, and extending the axial dimension of the detector array. For example, a typical whole-body ring system can realize an increase in the true sensitivity by up to a factor of 5 (for brain imaging) by removing the axial collimation. The penalty is a large increase in the acceptance of scattered photons (scatter fractions increasing by factors of 3 to 4) and increased singles rates from activity outside the field of view (FOV) of the system. We discuss some of the options for scatter correction and other issues in machine performance later in this chapter. First, we review the basics of detector designs used in PET systems.

II. DETECTOR DESIGNS

Early PET systems (Phelps *et al.*, 1978; Ter-Pogossian *et al.*, 1978; Brooks *et al.*, 1980) used one photomultiplier tube (PMT) per scintillation crystal. There are several major limitations to this approach. For high spatial resolution, one needs to use small crystals and existing PMTs are too large to allow a full ring of very small crystals; also, it becomes difficult or impossible to make multiring systems. For a large number of crystals, this type of design also leads to a large number of electronic channels and PMTs, thus increasing the cost of the system.

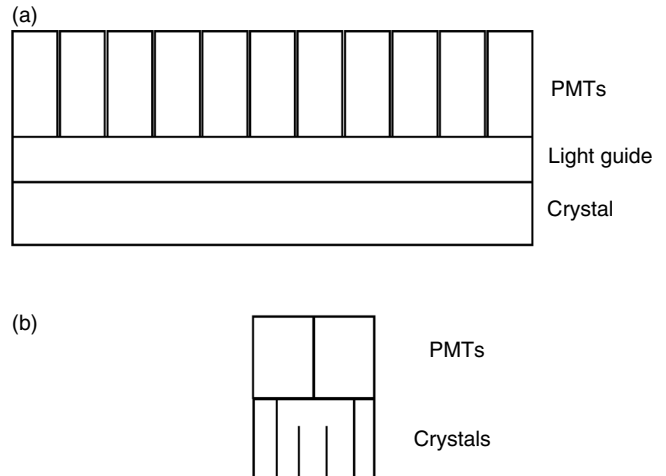


FIGURE 5 The major crystal-PMT decoding geometry options currently in use. (a) The continuous Anger-logic approach uses an array of PMTs to decode a large continuous crystal or an array of crystals. (b) The block detector uses four PMTs to decode an array of crystals with various combinations of reflectors and surface treatments between the crystals.

Alternative detector designs that shared crystals between PMTs began appearing in the 1980s. Examples of these designs can be found in the review article Muehllehner *et al.* (1986). Figure 5 shows two major design approaches currently in use. The first is based on the original Anger-logic approach (Karp *et al.*, 1990) with large area detectors viewed by an array of PMTs; the other uses smaller discrete crystals arranged in a block viewed by a limited number of smaller PMTs (Casey and Nutt, 1986).

The use of Anger-logic NaI(Tl) detectors for PET imaging (Muehllehner *et al.*, 1976) requires a thicker scintillation crystal than that normally used for single-photon imaging. The Philips Medical Systems C-PET scanner (Adam *et al.*, 2001) is a modern dedicated PET scanner that uses NaI(Tl) detectors. All manufacturers offer dual- (or triple-) headed NaI(Tl) cameras that can be used for either PET imaging (electronics set for coincidence detection) or single-photon emission computed tomography (SPECT) imaging (no coincidence and with collimators on detectors). Although a 3/8-in-thick detector stops over 90% of the gamma rays at 140 keV, it stops only ~10% at 511 keV. This, in turn, leads to only ~1% coincidence detection efficiency. For PET imaging, a 1-in-thick detector is normally used to achieve higher sensitivity; approximately 56% of the gamma rays at 511 keV are stopped, leading to 31% coincidence detection efficiency. Although a thicker detector leads to higher detection efficiency, the intrinsic spatial resolution degrades as the detector is made thicker. The loss of spatial resolution for thick detectors is mainly due to Compton scattering within the scintillator, which spreads the area over which the gamma-ray energy is deposited. Spatial resolution also depends on the design of the light guide that serves to spread the scintillation light to an appropriate number of

PMTs. It is desirable to restrict the spread of light to a small number of PMTs, because this will reduce the chance of event pile-up at higher count rates.

In addition to using a thicker scintillation crystal, modifications are required to the detector and the electronics used in large NaI(Tl) systems in order to allow higher count rates. The need for a very high count-rate capability in a PET scanner is not immediately evident. It is mainly due to the fact that a relatively low fraction of single-photon events are in coincidence and available for image generation. A high percentage of detected gamma rays are not in coincidence with another gamma ray but contribute to the singles count rate seen by the system. Many techniques used to achieve a high count-rate capability have been developed. These techniques include pulse shortening (Amsel *et al.*, 1969), local centroid positioning (Karp *et al.*, 1986), and the use of multiple trigger channels (Mankoff *et al.*, 1990). Pulse shortening is required because the scintillation decay time of NaI(Tl) is relatively long. The characteristic decay constant is 240 ns, which means that it takes about 900 ns to collect all the light. For 140 keV, a long integration time is used and an intrinsic energy resolution of 11% and spatial resolution of ~3.5 mm are achieved. At 511 keV, more than three times as much light is emitted in the scintillator, and one can afford to clip the electronic pulse corresponding to the light emission to approximately 200 ns and still achieve approximately 11% energy resolution. Even though the light from the first event continues to be emitted after 200 ns, the electronics can analyze another event after 200 ns, thereby reducing the dead time in the detector and increasing the count-rate capability.

The event-positioning electronics in most modern systems are digitally controlled at almost all levels. Once the PMT signals are digitized, the integration period is digitally controlled, as well as the number of PMTs included in the position calculation. Traditionally, the position of an event in an Anger camera (with continuous detector, as in Fig. 5a) is determined by calculating the centroid of the emitted light:

$$X = \frac{\sum_i (x_i S_i)}{\sum_i (S_i)}$$

where x_i is the weight associated with the i th PMT and S_i is the integrated PMT signal. A similar calculation is made to determine the orthogonal direction Y to achieve a 2-D position. In an analog circuit, the summation occurs over all PMTs, but with digital control one can specify the number of PMTs in the immediate vicinity of the scintillation event. With C-PET, for example, seven PMTs (in a 2D hexagonal pattern) are used to calculate the position and energy of each event. The local cluster of PMTs is determined by searching for the PMT with the highest signal. The local centroid calculation allows multiple events to be processed in the detector simultaneously, as long as they are spatially separated.

In addition to reducing pulse pile-up from the combination of pulse shortening and the local centroid calculation,

the electronic dead time is reduced by dividing the detector into multiple regions, each of which is connected to an independent set of electronics. For a coincidence event to be recorded, it is necessary for two trigger channels, from approximately opposite sides of the detector ring, to fire within a short period of time. Typically the coincidence-resolving time, referred to as 2τ , is 8 ns for NaI(Tl)-based PET systems. Multiple trigger channels in each detector allow simultaneous coincident events to be processed.

The large continuous crystal approach is generally not possible for a range of scintillators currently in use for PET scanner construction. In fact, a majority of the current PET scanners being built use discrete crystals or small blocks of scintillators rather than the large continuous crystal designs developed for NaI(Tl) systems. These scintillators that have higher stopping power (e.g., BGO, LSO, and GSO) can not currently be grown into large crystals and, with the exception of LSO, do not produce sufficient light output to achieve good spatial localization as a continuous detector.

For the small block arrays (Fig. 5b), a limited number (four) of small PMTs are used. The interface between the crystals is used to shape the light-spread function (LSF) to allow the decoding of crystal positions. The LSF can be controlled with different coupling compounds at the interface and surface finishing or by using different lengths of reflector between the crystals. For example, in the simplified block depicted in Figure 5b the outer crystals have reflectors running the full length of the block. Thus, any light produced in those crystals is detected in a single PMT. The remaining crystals have reflectors going only partway and coupling compound the rest of the way. Light from these crystals will be shared by the PMTs. By changing the lengths of the reflectors, the amount of light shared between the PMTs can be controlled. Figure 6 shows a 2D crystal map from a detector block using a 6×6 array of BGO crystals. Four PMTs are placed over the crystals in a rectangular pattern:

$$\begin{bmatrix} A & B \\ C & D \end{bmatrix}$$

To form the ratios, the two PMTs across the top of the block are summed for the x value ($A + B$) and the two PMTs along the left side are summed for the y value ($A + C$). For both ratios, the sum of the signals from all four PMTs are summed to obtain the denominator:

$$x = \frac{A + B}{A + B + C + D}; \quad y = \frac{A + C}{A + B + C + D}$$

Due to variances in PMT performance, normal production techniques, and the methods to shape the LSF, the light isocontour plots are not symmetric around the block. Search routines are used to find the minima between the peaks (the thick white lines in Fig. 6) and any events within a given region are assigned to the crystal position associated with

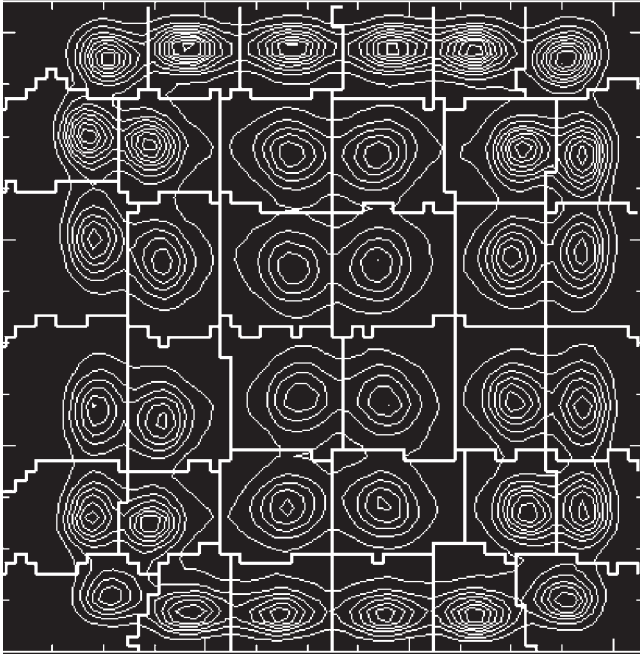


FIGURE 6 A 2D block map of a 6×6 BGO crystal array viewed by four PMTs. The relative light output is indicated by the isocount curves. The heavy white lines indicate which regions will be assigned to each crystal position.

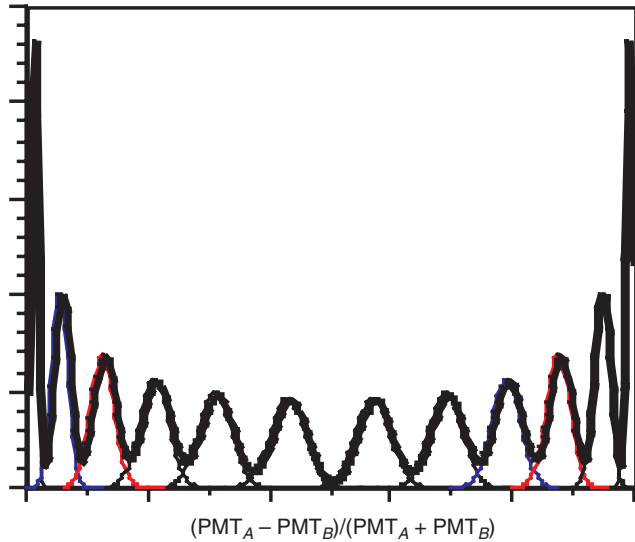


FIGURE 7 Plot of the PMT ratio (two PMTs) for a linear array of 12 LSO crystals. The y axis is the relative number of events detected.

that region. The graph in Figure 7 shows crystal identification (the ratio of the difference in the PMT outputs over the sum of the PMT outputs) versus source position for an experimental detector block using LSO crystals. This block allows the decoding of 12 crystals with two PMTs. As can be seen in the plot, the proper shaping of the LSF allows relatively easy decoding of the crystals. Careful inspection also

reveals that there is some overlap between adjacent crystals (the ratio does not go to zero between the peak centers).

Another example of the block design is the HR+ block (Adam *et al.*, 1997), which uses an 8×8 array of 4.5×4.1 mm² crystals in a block with four 19-mm PMTs performing signal readout. A modification of the block design is the quadrant-sharing block design (Wong *et al.*, 1995), which reduces the number of PMTs needed for a given number of crystals and has been used with arrays of smaller crystals than those used, for example, in the HR+ design. For example, one quadrant-sharing design uses blocks that make up a 7×7 array of 2.8×2.8 mm² crystals. The 19-mm PMTs now straddle four block quadrants so that each block is still viewed by four PMTs but each PMT is also shared by four blocks. The decoding ratio (number of crystals/PMT) of the standard block is 16:1, whereas that of the quadrant-sharing block is 49:1. However, because the PMTs are shared by four blocks, an interaction in any given block of the quadrant-sharing design will deaden the adjacent (eight) blocks. In comparison, an interaction in a block of the standard block design will deaden only one block area. Thus, the dead time of the quadrant-sharing block design using 2.8×2.8 mm² crystals will be more than a factor of 2 higher than that of the standard HR+ block design. The LSO panel detectors developed by CPS Innovations also use a quadrant-sharing block design, using 4×4 mm² crystals.

A different approach is used for the GSO detector modules used in the Phillips Allegro scanner. Although the detector uses discrete crystals ($4 \times 6 \times 20$ mm³), the crystals are not grouped into small blocks, and the light guides for each of the 28 detector modules are coupled to allow light sharing between adjacent modules. Rather than using four PMTs to decode each event, the Allegro design uses seven 39-mm diameter PMTs in a hexagonal arrangement. However, unlike the block detector, the group of seven PMTs does not correspond to a specific block of crystals because as it is chosen electronically from among a large array of PMTs coupled to the detector.

III. TOMOGRAPHY SYSTEM GEOMETRY

As we have discussed, current detector module designs use either large continuous NaI(Tl) crystals or arrays of discrete crystals. The NaI(Tl) systems offer a lower price due to the lower cost of the scintillator and the use of fewer electronics channels, whereas the discrete crystal machines offer higher sensitivity due to the higher stopping power of the scintillators used (e.g., BGO, LSO, or GSO) and much higher count-rate performance (e.g., lower dead time and less pulse pileup). In either case, the detectors can be configured as full rings that completely surround the patient or as partial rings with rotational motion to obtain the

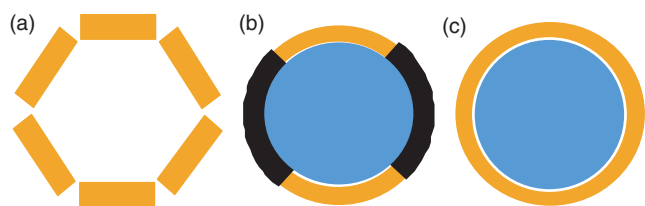


FIGURE 8 The three basic geometries found in modern dedicated PET systems. (a) Array of large detectors, either continuous detectors (flat or curve-plate NaI(Tl)) or plates of discrete crystals. (b) Partial ring of detector blocks that rotates. (c) Full ring of discrete crystals configured as small blocks or larger detector modules.

needed angular sampling (Fig. 8). Current designs with NaI(Tl) use either six large 25-mm-thick curve plates (full ring) or SPECT systems with two or three detector heads with 18- to 25-mm-thick detectors (partial ring). Current discrete crystal designs use BGO (25–30 mm thick), LSO (typically 25 mm thick), or GSO (typically 20 mm thick) arranged in full or partial rings about the patient.

Full-ring NaI(Tl) systems are currently being built with an axial extent of 25 cm (Adam *et al.*, 2001). Because the NaI(Tl) system use continuous detectors, the axial sampling is determined by the intrinsic spatial resolution of the system and the choice in how the data are collected. These systems typically sort the data into 128 axial image planes (2 mm thick) for brain studies, and 64 axial planes (4 mm thick) for whole-body studies. These full-ring NaI(Tl) systems are operated exclusively in positron volume imaging (PVI) mode (also known as 3D mode) to achieve better sensitivity.

Full-ring discrete crystal systems currently all use BGO, LSO, or GSO. As described in the preceding section, some common block sizes include 6×6 arrays of $4 \times 8 \times 30 \text{ mm}^3$ BGO crystals (GE Advance) or $6.25 \times 6.25 \times 30 \text{ mm}^3$ BGO crystals (GE Discovery ST) and 8×8 arrays of $6.75 \times 6.75 \times 20 \text{ mm}^3$ BGO crystals (Siemens/CTI EXACT) or $4.5 \times 4.8 \times 30 \text{ mm}^3$ BGO crystals (EXACT HR+). In addition, the ECAT ACCEL uses an 8×8 array of $6.75 \times 6.75 \times 25 \text{ mm}^3$ LSO crystals. The Phillips Allegro uses $4 \times 6 \times 20 \text{ mm}^3$ GSO crystals assembled in 28 modules that are optically coupled to one another and viewed by a hexagonal array of PMTs. All the dedicated stand-alone (i.e., not combined with computed tomography, CT, scanners) BGO and LSO systems have ring diameters of 80–90 cm and are equipped with removable axial collimators, allowing the systems to operate in either 2D or 3D mode. The GSO systems do not include axial collimators and only operate in 3D mode, as do the NaI(Tl) scanners. In addition, many of the PET/CT scanners now being offered (discussed later in this book) also do not include axial collimators, thereby allowing only 3D acquisition.

Discrete BGO and LSO systems are also available in partial-ring designs, the Siemens/CTI ECAT ART (BGO) and EMERGE (LSO). Because block detectors generally use

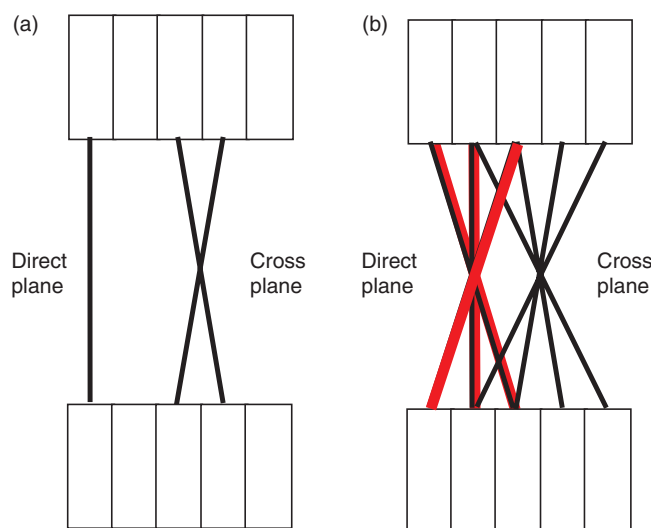


FIGURE 9 Two methods of binning 2D data in dedicated PET scanners with axial collimation. (a) High-resolution (HR) mode uses ring differences of 0 for the direct planes and ring differences of 1 for the cross planes. (b) To gain more sensitivity, data are most often binned in high-sensitivity (HS) mode. In this case the direct planes use ring differences of 0 and 2 and the cross planes use ring differences of 1 and 3. In both cases, the number of sinograms is $2n-1$, where n is the number of detector rings.

smaller PMTs than the continuous crystal designs, they are more expensive (due to the increased number of PMTs and electronic channels). In an effort to reduce the cost of these systems, partial-ring designs were developed. These machines essentially take a portion of the blocks used in a full-ring system and mount them on a rotating plate. Current designs use blocks with 8×8 arrays of $6.75 \times 6.75 \times 20 \text{ mm}^3$ (BGO) or $6.75 \times 6.75 \times 25 \text{ mm}^3$ (LSO) crystals. A typical arrangement uses 66 blocks arranged with three blocks in the axial direction providing 24 partial rings of crystals and an axial extent of 16.2 cm. The ring diameters are 82.5 cm. To compensate for the loss of sensitivity from only using partial rings of detectors, these systems operate only in PVI mode.

When a system operates in 2D mode (axial collimation), the data normally are binned directly into stacked 2D sinograms. Figure 9 illustrates the two most common methods of binning the data when axial collimation is used. One scheme, termed in the GE Advance the high-resolution mode, uses ring differences of 0 for the direct planes and ring differences of 1 for the cross planes (Lewellen *et al.*, 1996). To gain more sensitivity, data are often binned in what is often termed high-sensitivity mode. In this case the direct planes use ring differences of 0 and 2 and the cross planes use ring differences of 1 and 3. In both cases, the number of sinograms is $2n - 1$, where n is the number of detector rings. Other schemes that combine the detector data into sinograms achieve a different trade-off between sensitivity and resolution.

When the axial collimators are removed, the system collects full 3D data sets and operates as a PVI system. As

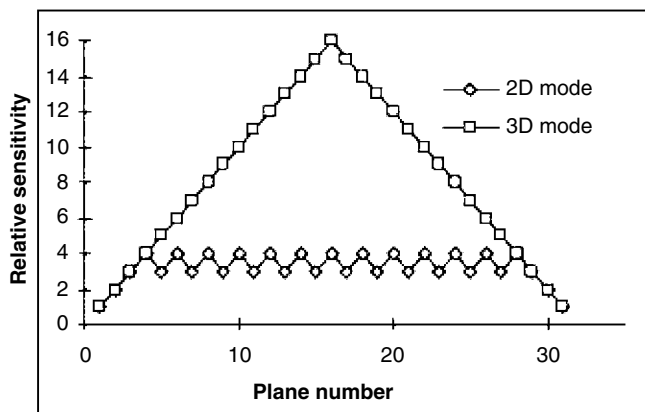


FIGURE 10 Comparison between 2D (axial collimation in place) and 3D (axial collimation removed) sensitivity.

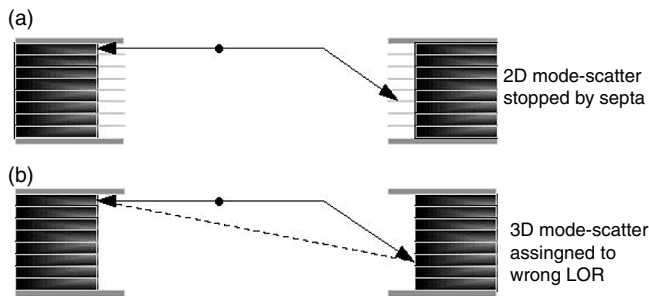


FIGURE 11 Illustration of the difference in axial acceptance of scattered events between 2D and 3D modes of operation of a PET system. (a) 2D mode, scatter stopped by septa. (b) 3D mode, scatter assigned to wrong LOR.

we have already noted, PVI offers an increase in sensitivity compared to 2D acquisitions (Fig. 10). However, there are some limitations to operating a system in 3D mode. Because the increased sensitivity is not uniformly distributed axially, the sensitivity advantage of 3D falls off rapidly as one approaches the edges of the axial FOV. The removal of collimation also increases the number of scattered events detected by the detector array (Fig. 11). The increase in scattered radiation depends on the lower-level energy discriminator (LLED), which in turn depends on the energy resolution of the system. A higher LLED setting can be used with scintillators that have better energy resolution. Typically, the LLED is set at 300–375 keV for BGO systems, 350–400 keV for LSO systems, 420 keV for GSO systems, and 435 keV for NaI(Tl) systems. The removal of the collimation also allows more photons from outside the axial FOV to be detected (Fig. 12). This increase in the number of single events detected versus the number of coincidence events detected leads to higher dead time and randoms rates.

In all system designs, the ring diameter and design of end shields and collimators have an impact on the accepted

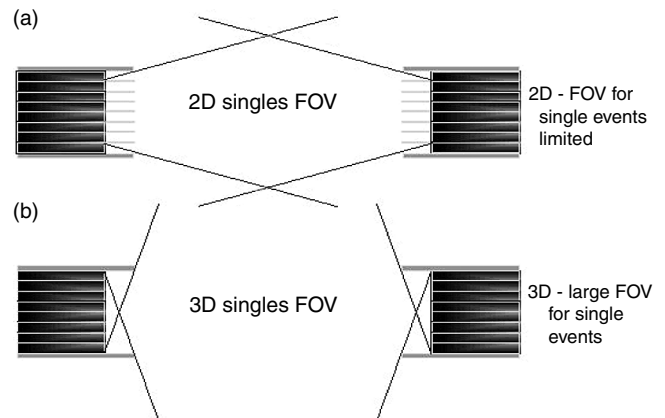


FIGURE 12 Illustration of the increase in the singles axial FOV in 3D mode (b) compared to the limited FOV in 2D mode (a) in a PET system. The increased singles FOV results in a higher randoms rate for the same amount of activity.

scatter and the trues-to-singles ratio (the number of true coincident events processed compared to the number of single events the detector must process). Thus, the system designer has to balance the increase in trues with larger axial FOVs and smaller detector rings against the impact of the out-of-field activity on the system dead time and accidental coincidence rate. Figure 12 illustrates the significant increase in the singles rate, and therefore randoms rate as well, that result from activity outside the FOV in 3D systems (without septa) compared to 2D systems (with septa). Of course, the system performance also depends heavily on the design of the supporting electronics, in addition to the detector configuration. As discussed later, another important parameter in 3D is the speed of the scintillator because fast scintillators such as LSO and GSO allow the use of a smaller coincidence window (2τ), which in turn leads to lower random coincidence rates.

IV. POSITRON EMISSION TOMOGRAPHY SCINTILLATORS

Table 5 lists some of the properties of scintillators that have been used for PET imaging systems. Other than BaF₂, which was used in early time-of-flight systems (Wong *et al.*, 1984), all these scintillators are currently in use in commercial PET systems. System designers want a scintillator that has a very high light output, has a high energy resolution, is very dense with a large photoelectric cross section, has a fast decay constant, is nonhygroscopic, and is easy to grow into large crystals. Unfortunately, no single scintillator has all these ideal properties. We have already mentioned that the high light output of NaI(Tl) makes it a good choice for large area detectors. The fact that it can be grown into large crys-

Table 5 Properties of Scintillators Used in PET

	NaI(Tl)	BaF ₂	BGO	LSO	GSO
Effective atomic number (<i>Z</i>)	51	54	74	66	59
Linear attenuation coefficient (cm ⁻¹)	0.34	0.44	0.92	0.87	0.62
Index of refraction	1.85	–	2.15	1.82	1.85
Light yield (% NaI(Tl))	100	5	15	75	30
Peak wavelength (nm)	410	220	480	420	430
Decay constant (ns)	230	0.8	300	40	65
Fragile	Yes	Slight	No	No	No
Hydroscopic	Yes	No	No	No	No

tals at modest cost is another primary reason for its use in imaging systems. BGO has been popular due to its high stopping power and density. However, its low light output precludes its use for large area detectors with large PMTs. GSO and LSO both have good stopping power and fast decay, which lead to higher count-rate capability. However, due to their very high melting point (~2000°C) these crystals generally cost significantly more than either NaI(Tl) or BGO.

Currently, the high-end PET scanners being offered are all based on BGO, LSO, and GSO. Efforts are ongoing at many laboratories to develop better scintillators and reduce the cost of growing the more interesting candidates. A list of current candidates is beyond the scope of this chapter, but there are many exciting materials under development that may replace the current scintillators in future scanners (see van Eijk, 2002).

The intrinsic performance of these scintillators relates directly to overall scanner performance. For example, the energy resolution of a scintillator is dependent on its light output and the intrinsic scintillator resolution, which is a function of the variability in the light yield (e.g., how much light gets out of the scintillator as a function of where the scintillation occurs in the crystal). A high light yield from a scintillator normally improves the energy resolution for the detector because it reduces the Poisson noise of the PMT signal. Good energy resolution allows the use of a narrow photopeak energy window (high LLED) to maximize true coincidences and minimize scatter (and randoms) in the image, thereby improving contrast. High scintillator light yield also yields a high crystal decoding ratio, which permits the discrimination of smaller crystals with fewer, larger PMTs. The high density of a crystal (high linear attenuation coefficient) increases the detector sensitivity to coincident events. A high linear attenuation coefficient for a scintillator will also help reduce the parallax error in the scanner due to the reduced variability of the DOI of incident gamma rays in the detector. A short signal decay time helps reduce the width of the coincidence timing window (2τ), thereby reduc-

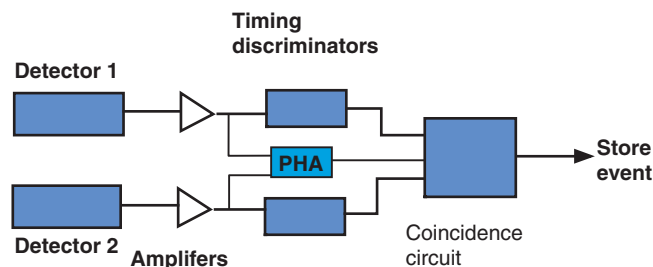


FIGURE 13 Basic electronic components for a PET system. The amplifiers integrate the detector signals. The pulse-height analyzer (PHA) selects the energy range of events to be accepted. The timing discriminators generate the timing pulse for the coincidence circuit.

ing the rate of random coincidences within the scanner. Very short signal decay time and very good coincidence timing resolution (≤ 600 ps) are the main requirements for a scintillator to be used in a time-of-flight scanner.

V. POSITRON EMISSION TOMOGRAPHY SYSTEM ELECTRONICS

Figure 13 shows the basic components of the electronics system for a tomograph. The signals from the PMTs are integrated. In a BGO block system, which typically has many PMTs and readout channels, the major contribution to dead time is from these integrating amplifiers. The amplified signals are routed to a pulse-height analyzer (PHA) to select the energy range for the events to be processed. The signals also go to timing discriminators to generate timing signals for the coincidence system. Normally, the timing discriminators include lower-energy discriminators to reject events that have too low an energy to be passed by the PHA. Thus, the amplifiers see the full detector count rate, which is generally much higher than the output of the timing discriminators. For PET systems with large area detectors, each detector element (the crystal) subtends a large solid angle and has a high singles rate. As a result, the maximum count-rate performance of large area detector systems is usually limited by the pulse pile-up in the detectors, even when high count-rate techniques are employed (see previous discussion regarding pulse shortening, local centroid calculation, and multiple triggers). In a block system with discrete crystals, each detector element (the block that sends signals to an amplifier) subtends a relatively small solid angle. In these systems with many readout channels, the count-rate performance is usually limited by the random event rates rather than detector dead time.

The actual electronics in a full tomograph are more complicated than indicated in Figure 13. There are modules to decode the event position, to correct for the variance in photopeak position in various detector elements, to collect

data for dead-time correction, and to sort the data and store it on disk. Major aspects of the system design are the details of the implementation of the coincidence electronics and the method to perform randoms correction. There are two standard approaches for measuring the randoms. Figure 14 illustrates the delayed-window approach. The number of events is plotted versus the time difference between detection of events by two detectors. The peak represents the prompt events *plus* random events. Our goal is to remove the random events from the prompt window. A delayed window can be defined that only samples random events. Data from the randoms window can either be saved or scaled and subtracted from the prompt window data during acquisition. This latter option (real-time subtraction) is often used by commercial PET systems. The disadvantage of real-time subtraction is that the randoms data for any given LOR may have a high variance. Saving the randoms data and using appropriate variance-reduction techniques can lead to a better quality data set. Another approach to reducing the variance is to calculate the randoms from the single event rates in the detectors. Because the singles rates are always much higher than the coincidence rates, the data have a low variance. The randoms can then be calculated using the relation:

$$R = 2\tau S_1 S_2$$

where τ is the time resolution of the system (and 2τ is the coincidence time window), and S_1 and S_2 are the singles rates of two detectors defining a given LOR. The major complications of this approach are (1) proper accounting of all sources of dead time so that the correct randoms rate is calculated for subtraction from the prompt data and (2) accounting for any variance in τ between different detectors. Whatever approach is used, the system designer usually separates the electronics into a series of parallel channels to reduce dead time in the coincidence electronics.

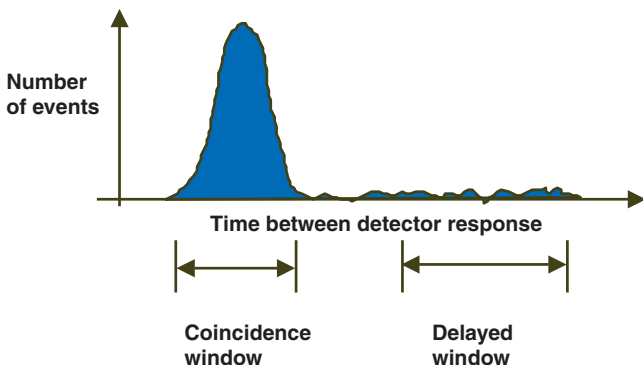


FIGURE 14 Time spectrum of the coincidence events in a PET scanner. The peak is termed the coincidence window and represents prompts + randoms. The delayed window samples the randoms distribution.

Once the data have passed the coincidence system, they are usually histogrammed into sinograms in high-speed memory. Such an arrangement easily allows dynamic studies to be acquired. Once the data have been saved to disk, the designer again has several options. The current system designs all use standard UNIX or Windows workstations to operate the scanner and function as image-display stations. When the data are reconstructed, two approaches are currently used. One approach uses a central reconstruction engine—a central computer that supports reconstruction requests from all workstations. Such an architecture typically uses a multi-CPU array of processors. The other approach is to let each workstation reconstruct its own images, with or without additional computational power added to the standard workstation. The data processing/reconstruction software must take into account many corrections, including dead time, randoms (if not subtracted during acquisition), detector normalization (correction for detector efficiency and geometric factors), scatter, and attenuation.

VI. ATTENUATION CORRECTION

A particular advantage of PET imaging is that attenuation correction factors do not depend on the location of a source along a given LOR. Consider Figure 15. For an event to be registered, both gamma rays from the decay must be detected. Thus, the probability that a gamma ray will reach detector 1 is:

$$p_1 = e^{-\int_0^{x'} \mu(x) dx}$$

and the probability that a gamma ray will reach to detector 2 is:

$$p_2 = e^{-\int_{x'}^a \mu(x) dx}$$

The total probability that the pair of gamma rays is detected is then:

$$p_d = p_1 p_2 = e^{-\int_0^a \mu(x) dx}$$

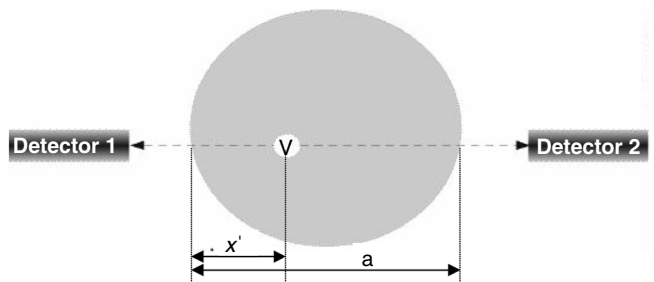


FIGURE 15 Attenuation in PET. The attenuation correction does not depend on where along the LOR the positron decay occurs.

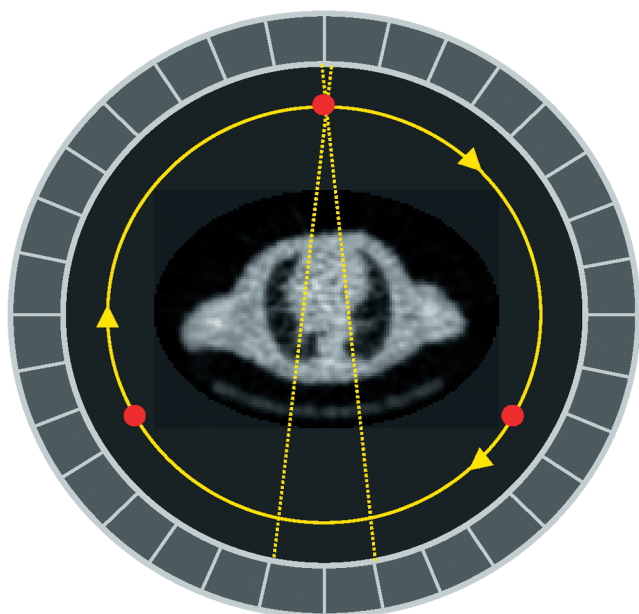


FIGURE 16 A configuration of transmission sources in a dedicated PET scanner. A rotating rod or point source (depending on whether the system is in 2D or 3D mode of operation) is rotated around the patient. Systems with one, two, or three rod/point sources have been developed commercially.

Thus, the probability of detection (of not being attenuated) is independent of the position X' of the decay site along the LOR. If a source is placed outside of the patient (Figure 16), then the attenuation measured along any LOR with the source will be the proper correction for the emission data (the transmission scan). The correction is simply measured by taking the natural logarithm of the ratio between the transmission scan and a blank scan (a scan with the external source without any objects in the scanner's FOV).

There are several options for acquiring the transmission data. Most of the dedicated ring scanners use a coincidence-based attenuation scan (Carroll *et al.*, 1983; Daube-Witherspoon *et al.*, 1988). The data are acquired in coincidence mode as the external source rotates around the scanner FOV. In this mode of operation, the data are normally restricted (or gated) to events where the LOR between the detector pair also goes through the current position of the external source. In that way, gamma rays that are scattered within the FOV are rejected (they do not pass through the position of the external source at the time of decay). If there is activity within the object during the transmission scan (postinjection transmission scanning), the use of the gated-source approach also rejects most of the events arising from the isotope within the patient. Only small corrections are needed from an emission scan to measure the attenuation correction factors accurately. Systems using

this approach have been built using one, two, or three rotating rod sources, usually containing several millicuries of ^{68}Ge . One disadvantage of this approach is that it puts a high-activity source very close to detectors. The near detector (the detector closest to the source) will experience a large dead time, which limits the count rate that can be achieved in the coincidence data acquisition. The use of two or three rods in modern machines is a partial solution to the problem (distributing the activity so the count rate due to any single rod is lower). However, transmission scan times are still long (typically 10–15 min) if the data are used directly. This scan time corresponds to a single bed position, which typically covers an axial extent equal to the axial FOV. Therefore, to acquire a whole-body scan (approximately 70 cm), typically seven bed positions are acquired.

To shorten the overall scan time, several approaches have been developed. One method to reduce the transmission scan time is to ignore the near detector and collect the data in singles mode (disable the coincidence system). Such an approach allows the use of higher activity sources (5–20 mCi) to acquire high-quality data in < 1 min per FOV. The designer of such a system can also use a long-lived source such as ^{137}Cs (30 years) because the source does not need to be a positron emitter—an advantage in terms of cost of operation of the scanner (Karp *et al.*, 1995). The disadvantage of this is that the attenuation data are contaminated by scatter and correction for events from the isotope already in the patient; however, a correction can be made to avoid bias errors in the attenuation correction. Another correction must be made to account for the fact that the measured attenuation coefficients from ^{137}Cs at 662 keV are approximately 10% lower than those for 511 keV, the energy of the emission gamma rays from a positron emitter (Smith *et al.*, 1997). These systems use segmentation to identify different tissue types in the attenuation images and then reassign pixels to the proper values for those tissues (Bilger *et al.*, 2001). The segmented data can then be used for calculating the attenuation correction factors. This approach has also been applied to coincidence-mode data (Xu *et al.*, 1994; Weng and Bettinadi, 1993) with the result that transmission scan times of 1–3 min can be realized with either singles- or coincidence-mode transmission scan schemes.

Another approach is to use a small reference detector in conjunction with a collimated coincidence source that is rotated around the patient (Watson *et al.*, 2001). Using a fast scintillator for the reference detector (e.g., LSO), fast count rates can be obtained with minimal problems with emission contamination from the patient. This technique has been used in some research systems developed by CPS Innovations.

Still another approach to the measurement of transmission data is to combine a CT scanner with a PET system. The resulting data are taken at an energy that is very differ-

ent from 511 keV, so the data must be scaled to use for attenuation correction of the emission data. More information on this approach is included in Watson *et al.* (Chapter 11 in this volume).

VII. SCATTER CORRECTION

Scatter correction techniques include integral transform, function fitting, energy-based subtraction, and analytic calculation (Bergstrom *et al.*, 1983; Grootoonk *et al.*, 1991; Bailey and Meikle, 1994; Ollinger, 1995). The accuracy of each approach is dependent on, among other things, the mode of operation (e.g., 2D vs. 3D), the details of the scanner design and scintillator used, and the size of the object being scanned (e.g., brain vs. whole body). The integral transform method uses a simple function such as an exponential model for the scatter response to a point source within the object. The parameters for the model (usually amplitude and rate of fall-off) are normally derived from a series of phantom studies. To partially address the issue that the scatter response is not stationary and that the parameters are normally derived from simple cylindrical phantoms, the parameters are often modified by the measured attenuation length for a given LOR. Integral transform techniques are common for scanners operating in 2D mode, in which modest errors in scatter estimation (e.g., 10–20%) do not have a large impact because the overall scatter fraction (scatter/total events) is also modest (10–20%). However, in 3D mode, errors in scatter estimation have a much larger impact because the scatter fraction is significantly larger (35–60%).

The function-fitting method fits a function to the data acquired from outside the object. Here, the assumption is that all the events outside the object after randoms correction are due to scatter. In this approach, a modified Gaussian or parabolic function is often used to describe the scatter profile in sinogram space, and that function is fitted to the data using the events outside the object. As in the integral transform approach, the shape of the function is normally determined from a series of simple phantom studies. Although this method is simple, it has the advantage that it takes into account activity outside the FOV, unlike the integral transform method. The fitting method, however, does not take into account local variations of the activity distribution or attenuation; thus, it provides only a smooth estimate of the scatter distribution.

Energy-based approaches can take many forms. The most common has been to acquire data with two energy windows, one over the photopeak and one over the Compton scatter region (Grootoonk *et al.*, 1991; Harrison *et al.*, 1991). The assumption is that a scaled subtraction of the Compton window events from the photopeak window events for each

LOR will provide the proper scatter correction. Part of the attraction of this approach in 3D is that the energy information, in principle, should reflect the impact of scatters from activity both outside and inside the FOV. However, in dedicated PET systems, the Compton region of the energy spectrum is dominated by multiple-scattered and large-angle single-scattered gamma rays. The spatial distribution of these gamma rays is different from the small-angle single scatters that dominate the scattered events accepted into the photopeak window. Thus, the parameters derived for the dual-energy window approach are object-dependent and can lead to inaccuracies, particularly in body imaging. A variant is to place a small window just on the high side of the energy peak (Adam *et al.*, 2000). This approach provides a better estimate of the correct spatial distribution, but it is very sensitive to small changes in PMT gains and, as a result, difficult to implement. A third energy-based approach is to acquire data in several energy windows and use a model of the unscattered events and various types of scatter to deconvolve the energy spectrum and extract the unscattered events. The disadvantages of this approach are that it requires a great deal of data to be acquired and the resulting arrays are sparse, making the accurate extraction of the unscattered events very difficult.

For 3D PET, another approach that has been tried is to acquire short 2D scans in which the scatter correction is reasonable and then use the differences between the 3D and 2D scans to estimate the 3D scatter correction. However, this approach has not been pursued for most scanners and, instead, a scatter correction based on analytic calculations of the single scatter events is gaining acceptance. Using the Klein-Nishina formula, the algorithms calculate the single scatter events starting with the attenuation data and an initial reconstruction of the emission data (Ollinger, 1995; Watson *et al.*, 1996). Because the original data included scatter, the algorithms are normally iterative—using the initial scatter calculation to produce a scatter sinogram for comparison to the original data. Based on that comparison, the estimated true distribution is updated and a new scatter calculation made (Fig. 17). Implementations with or without explicit estimates of multiple scatters have been used. To account for the impact of activity from outside the FOV, two approaches have been used. One is to calculate the scatter correction and then scale it to force the mean value of events outside of the object (in sinogram space) to be zero. The other approach is to include short scans of the volumes on either side of the volume being reconstructed. Because the algorithms generally undersample the data fairly coarsely, a small amount of data from the overscanned areas is required. Some variations of this algorithm work in image space rather than sinogram space. This analytic scatter approach (often referred to as model-based corrections) is still an area of development, but it has already been implemented on many dedicated PET systems.

VIII. NOISE EQUIVALENT COUNT RATE

We have already looked at some aspects of comparing 2D to 3D imaging modes in PET scanners. 3D mode greatly

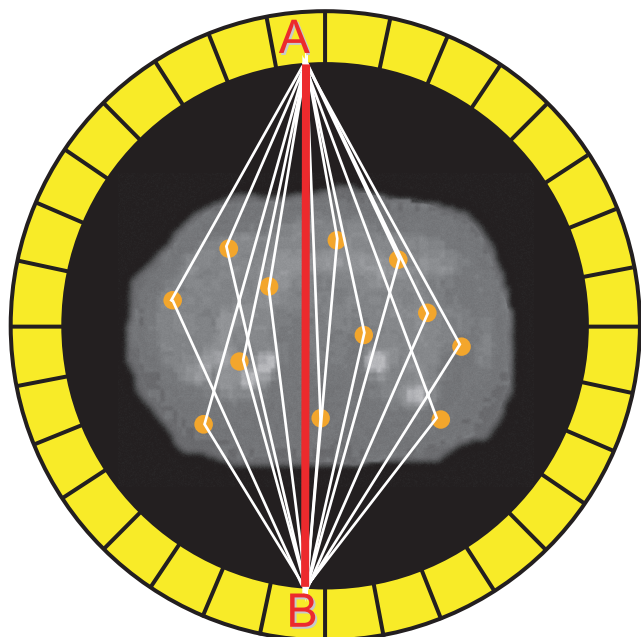


FIGURE 17 The model-based scatter correction defines the activity distribution from the emission image and the scattering medium distribution from the transmission image. The scatter points are distributed randomly in the volume, and the contributions of scatter are calculated using the Klein-Nishina formula for each selected LOR (AB).

improves the sensitivity for any scanner design, but it comes at the cost of nonuniform axial sensitivity, increased scatter fraction, and increased impact of activity outside the FOV. One measurement that has been used to give some insight into the quality of the primary data is the noise equivalent count (NEC) rate (Strother *et al.*, 1990). Although this metric does not directly relate to final image quality, it does demonstrate the impact of dead time, randoms rates, and scatter on the overall ability of the scanner to measure the true events count rate. Generally, the NEC is defined as:

$$\text{NEC} = \frac{T^2}{T + S + KR}$$

where T is the true count rate, S the scatter count rate, R the randoms count rate, and K is a factor that depends on the method used for randoms correction. In general, the real-time subtraction of randoms leads to the largest variances thus $K = 2$ is often used for real-time subtraction, whereas $K = 1$ is used when the randoms have first been smoothed before subtraction. Although a varying K is often used to distinguish among the different methods of randoms subtraction, this approach is normally not taken with scatter subtraction because it is more difficult to generalize the impact of the scatter correction accuracy on NEC.

Figure 18 shows the count-rate curves, the NEC for both the NEMA NU2 1994 (Karp *et al.*, 1991) and 2001 standards (Daube-Witherspoon *et al.*, 2002). The 1994 standard uses a 20-cm diameter by 19-cm long cylindrical phantom, which is representative of brain imaging. The 2001 standard uses a 20-cm diameter by 70-cm long phantom, which is more appropriate for whole-body imaging. This measurement is used so that the impact of out-of-field activity

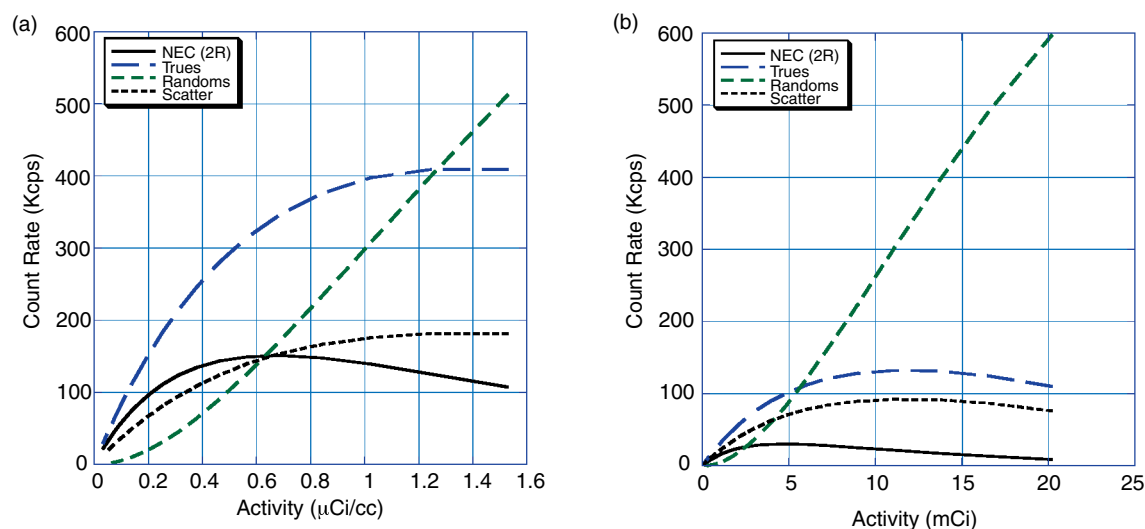


FIGURE 18 An example of noise equivalent count (NEC) rate for a dedicated PET scanner. (a) Data taken according to the NEMA 1994 protocol (20-cm-diameter \times 19-cm-long cylinder of activity). (b) Data taken with the 2001 protocol (line source in a 20-cm-diameter \times 70-cm-long cylinder). The data are from a BGO scanner with a lower energy threshold of 375 keV.

is included, as occurs naturally with whole-body patient studies. The NEC curves also illustrates the impact of randoms as the activity is increased. Families of such curves can provide some insight into the impact of different activity distributions on a given scanner's data collection (e.g., different body sizes and activity levels).

IX. FUTURE TRENDS

As we noted at the beginning of this chapter, system designers are always looking at ways to improve spatial resolution, and these generally require improvements in system sensitivity in addition to higher resolution detector arrays. One technology that aids in this quest is DOI detector systems. A DOI system is designed to give information about the depth in the crystal at which an interaction takes place. The system designer can then exploit that information to correct for parallax errors, allowing a reduction in the system ring diameter. Reducing the ring diameter allows either a potential reduction in cost (fewer scintillator and readout channels) or an extension of the axial FOV. In either case, there will be an increase in sensitivity due to the larger solid angle subtended by the detector array. Figure 19 depicts one approach being developed (Saoudi *et al.*, 1999). By using scintillators with different decay times, it is possible to select between different detector elements using pulse-shape discrimination (PSD). Systems with up to four different layers have been proposed. Systems with two layers (e.g., LSO with different time constants, or LSO/GSO and LSO/NaI(Tl) combinations) have been built (Schmand *et al.*, 1999). A second approach is illustrated in Figure 20. In this case, the detector surface

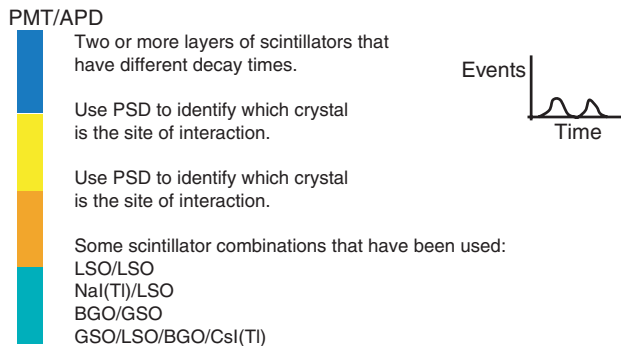


FIGURE 19 Depth of interaction by pulse shape analysis. Stacks of two or more layers of crystals with different timing properties allow the determination of which crystal is the source of the signal, based on analysis of the signal decay time, of pulse-shape discrimination (PSD). Some scintillator combinations that have been used are YLSO/LSO, NaI(Tl)/LSO, and BGO/GSO. The signals have been collected with PMTs, and avalanche photodiodes (APD).

is modified to force a different efficiency of light collection with depth, effectively causing the photopeak position to change with depth. Although some early development was done on this approach, it has not been adopted for any full systems designs thus far.

A third approach, that of exploiting how light is shared in the detector block, is illustrated in Figure 21. Three main designs have been developed. The first uses two layers of crystals that are offset, allowing the decoding of the crystal layer by which photocathodes in a multicathode PMT receive light (Vaquero *et al.*, 1998). The second uses two light collectors at either end of the crystals (usually an array of photodiodes coupled one on one to the crystals and a large-area PMT coupled to many crystals). The ratio of the light collected at each end is translated into the DOI location (Moses and Derenzo, 1994). The third uses surface treatments to change the sharing of light between two or more crystals as a function of the depth (Miyaoaka *et al.*, 1998).

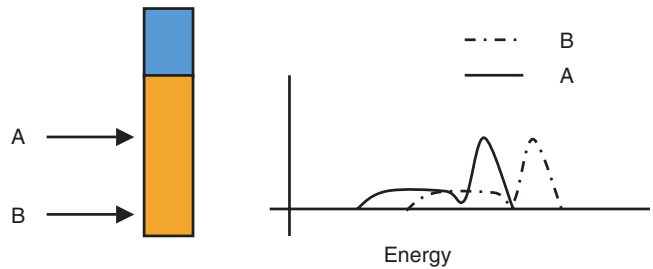


FIGURE 20 Depth of interaction by using the change of light collection with depth in long narrow crystals. The photopeak shift is related to the depth, as demonstrated by events incident at two depths, A and B.

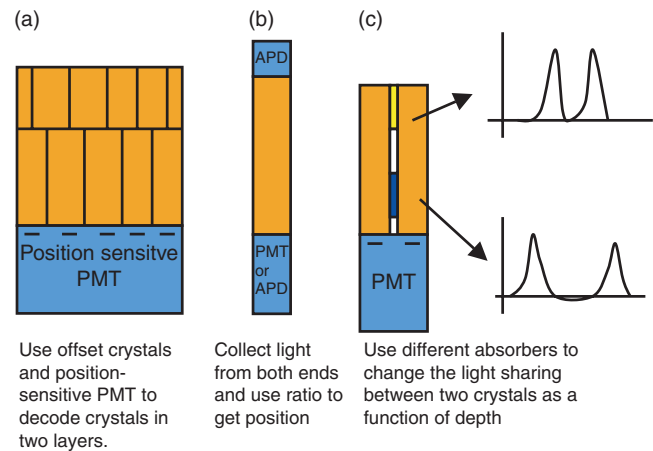


FIGURE 21 Depth of interaction by light sharing. The distribution of light is used to locate the depth of interaction with the array. (a) Using offset crystals and mutlianode PMTs to determine which crystal was the source. (b) Using PMT and APD at opposite ends of a crystal to measure the light ratio at both ends of the crystal to locate the interaction point. (c) Using different absorbers to modify the sharing of light between crystals to determine the interaction point by looking at the ratio of light between PMTs.

In this approach, the ratio value normally used for determining which crystal is the source of the interaction is also used to determine the DOI (the peaks, such as illustrated in Fig. 6, shift within the crystal zones as a function of the DOI). All three of these light-sharing approaches are being developed for possible use in imaging systems.

Another area of design that is active is the development of multimodality scanners. Currently, systems that combine a dedicated PET system with a CT scanner are in production. These systems generally use one detector array for PET imaging and a second, positioned opposite from an X-ray tube, for the CT scanning. Other laboratories are looking into the possibility of developing detector stacks that will allow a single detector array to function for several different modalities (X-ray, SPECT, and PET).

The designs for PET systems seem to be separating into three main groups of applications: (1) small animal imaging, (2) neurological imaging, and (3) whole-body imaging. This is largely due to the widely varying design criteria these different applications entail. Whole-body imaging is the application in which the majority of commercial system development is taking place, although there are also recent interest and development in small animal systems. The small animal systems can take advantage of new, costly scintillators because they generally need small volumes of detector material compared to a human whole-body scanner. To some extent, specialized neurological scanners can more easily take advantage of newer, more costly scintillators (e.g., LSO and GSO) (Weinhard *et al.*, 2002; Karp *et al.*, to appear) due to the reduction in scintillator volume compared to a whole-body system. Perhaps more important, a dedicated neurological scanner can reduce the ring diameter and select an axial FOV that provides significantly more sensitivity than can be obtained with a whole-body system. However, the cost of LSO and GSO has been reduced to the point that these materials are also being used in commercial whole-body scanner systems. The majority of the commercial development is likely to be in whole-body systems because the demand for body oncology imaging is high. The challenge is to increase the system's sensitivity to improve image quality (and decrease scan time) without increasing the cost of the system.

References

- Adam, L. E., Karp, J. S., Daube-Witherspoon, M. E., and Smith, R. J. (2001). Performance of a whole-body PET scanner using curve-plate NaI(Tl) detectors. *J. Nucl. Med.* **48**: 1821–1830.
- Adam, L. E., Karp, J. S., and Freifelder, R. (2000). Energy based scatter correction for 3D PET scanners using NaI(Tl) detectors. *IEEE Trans. Med. Imag.* **19**: 513–521.
- Adam, L. E., Zaers, J., Ostertag, H., Trojan, H., Bellemann, M. E., and Brix, G. (1997). Performance evaluation of the whole-body PET scanner ECAT EXACT HR+ following the IEC standard. *IEEE Trans. Nucl. Sci.* **44**: 1172–1179.
- Amsel, G., Brosshard, R., and Zajde, C. (1969). Shortening of detector signals in passive filters for pile-up reduction. *Nucl. Instr. Meth.* **71**: 1–12.
- Bailey, D., and Meikle, S. (1994). A convolution-subtraction scatter correction method for 3D PET. *Phys. Med. Biol.* **39**: 411–424.
- Beneditti, S. D., *et al.* (1950). On the angular distribution of two-photon annihilation radiation. *Phys. Rev.* **77**: 205–212.
- Bergstrom, M., Eriksson, L., Bohm, C., Blomqvist, G., and Litton, J. (1983). Correction for scattered radiation in a ring detector positron camera by integral transformation of the projections. *J. Comput. Assist. Tomogr.* **7**: 42–50.
- Bilger, K., Adam, L. E., and Karp, J. S. (2001). Segmented attenuation correction using Cs-137 single photon transmission. *2001 Conf. Rec. IEEE Nucl. Sci. Symp. Med. Imaging Conf.*
- Brooks, R. A., Sank, U. J., DiChiro, G., Friauf, W. S., and Leighton, S. B. (1980). Design of a high resolution positron emission tomograph: The neuro-PET. *J. Comput. Assist. Tomogr.* **4**: 5–13.
- Carroll, L., Kertz, P., and Orcut, G. (1983). The orbiting rod source: Improving performance in PET transmission correction scans. In "Emission Computed Tomography—Current Trends" (p. Esser, ed.), pp. ?. Society of Nuclear Medicine, New York.
- Casey, M., and Nutt, R. (1986). A multicrystal two dimensional BGO detector system for positron emission tomography. *IEEE Trans. Nucl. Sci.* **33**: 460–463.
- Daube-Witherspoon, M., Carson, R., and Green, M. (1988). Postinjection transmission attenuation measurements for PET. *IEEE Trans. Nucl. Sci.* **35**: 757–761.
- Daube-Witherspoon, M. E., Karp, J. S., Casey, M. E., DiFilippo, F. P., Hines, H., Muehllehner, G., Simcic, V., Stearns, C. W., Vernon, P., Adam, L. E., Kohlmyer, S., and Sossi, V. (2002). PET performance measurements using the NU 2–2001 standard. *J. Nucl. Med.* **43**: 1398–1409.
- Derenzo, S. E. (1979). Precision measurement of annihilation point spread distributions for medically important positron emitters. In "Proceedings of the 5th International Conference on Positron Annihilation" pp. 819–824.
- Grootoonk, S., Spinks, T. J., Michel, C., and Jones, T. (1991). Correction for scatter using dual energy window technique in a tomograph operated without septa. *1991 Conf. Rec. IEEE Nucl. Sci. Symp. Med. Imaging Conf.* **3**: 1569–1573.
- Harrison, R. L., Haynor, D. R., and Lewellen, T. K. (1991). Dual energy window scatter corrections for positron emission tomography. *1991 Conf. Rec. IEEE Nucl. Sci. Symp. Med. Imaging Conf.* **3**: 1700–1704.
- Hoffman, E. J., Huang, S., Plummer, D., and Phelps, M. E. (1982). Quantitation in positron emission computed tomography: 6 effect of nonuniform resolution. *J. Comput. Assist. Tomogr.* **6**(5), 987–999.
- Hoffman, E. J., and Phelps, M. E. (1976). An analysis of some of the physical aspects of positron axial tomography. *Comput. Biol. Med.* **6**: 345–360.
- Hoffman, E. J., and Phelps, M. E. (1978). Resolution limits for positron imaging devices. *J. Nucl. Med.* **18**: 491–492.
- Karp, J. S., Daube-Witherspoon, M. E., Hoffman, E. J., *et al.* (1991). Performance standards in positron emission tomography. *J. Nucl. Med.* **32**: 2342–2350.
- Karp, J., Muehllehner, G., Beerbohm, D., and Mankoff, D. (1986). Event localization in a continuous scintillation detector using digital processing. *IEEE Trans. Nucl. Sci.* **33**: 550–555.
- Karp, J. S., Muehllehner, G., Mankoff, D. A., Ordonez, C. E., Ollinger, J. M., Daube-Witherspoon, M. E., Haigh, A. T., and Beerbohm, D. J. (1990). Continuous-Slice PENN-pet: A positron tomograph with volume imaging capability. *J. Nucl. Med.* **31**: 617–627.
- Karp, J. S., Muehllehner, G., Qu, H., and Yan, X.-H. (1995). Singles transmission in volume imaging PET with a Cs-137 source. *Phys. Med. Biol.* **40**: 929–944.
- Karp, J. S., Surti, S., Freifelder, R., Daube-Witherspoon, M. E., Cardi, C., Adam, L. E., and Muehllehner, G. (to appear). Performance of a brain PET camera based on Anger-logic GSO detectors. *J. Nucl. Med.*

- Lewellen, T. K., Kohlmyer, S. G., Miyaoka, R. S., Kaplan, M. S., Stearns, C. W., and Schubert, S. F. (1996). Investigation of the performance of the General Electric ADVANCE positron emission tomograph in 3D mode. *IEEE Trans. Nucl. Sci.* **43**: 2199–2206.
- Mankoff, D. A., Muehllehner, G., and Miles, G. E. (1990). A local coincidence triggering system for PET tomographs composed of large-area position-sensitive detectors. *IEEE Trans. Nucl. Sci.* **37**: 730–736.
- Miyaoka, R.S., Lewellen, T.K., Yu, H., and McDaniel, D.L. (1998). Design of a depth of interaction (DOI) PET detector module. *IEEE Trans. Nucl. Sci.* **45**: 1069–1073.
- Moses, W. W., and Derenzo, S. E. (1994). Design studies for a PET detector module using a PIN Photodiode to measure depth of interaction. *IEEE Trans. Nucl. Sci.* **41**: 1441–1445.
- Muehllehner, G., Buchin, M. P., and Dudek, J. H. (1976). Performance parameters of a positron imaging camera. *IEEE Trans. Nucl. Sci.* **23**: 528–537.
- Muehllehner, G., and Karp, J. (1986). Positron emission tomography—technical considerations. *Sem. Nucl. Med.* 35–50.
- Nelleman, P., Hines, H., Braymer, W., Muehllehner, G., and Geagan, M. (1995). Performance characteristics of a dual head SPECT scanner with PET capability. *1995 Conf. Rec. IEEE Nucl. Sci. Symp. Med. Imaging Conf.* 1751–1755.
- Nohara, N., Tanaka, E., Tomitani, T., Yamamoto, M., and Murayama, H. (1985). Analytical study of performance of high resolution positron emission computed tomographs for animal study. *IEEE Trans. Nucl. Sci.* **32**: 818–821.
- Ollinger, J. M. (1995). Model-based scatter correction for fully 3D PET. *Phys. Med. Biol.* **41**: 153–176.
- Phelps, M. E., Hoffman, E. J., Huang, S. C., and Ter-Pogossian, M. M. (1975). Effect of positron range on spatial resolution. *J. Nucl. Med.* **16**: 649–652.
- Phelps, M. E., Hoffman, E. J., Huang, S. C., *et al.* (1978). A new computerized tomographic imaging system for positron-emitting radiopharmaceuticals. *J. Nucl. Med.* **19**: 635–647.
- Phelps, M. E., Huang, S. C., Hoffman, E. J., Plummer, D., and Carson, R. (1982). An analysis of signal amplification using small detectors in positron emission tomography. *J. Comput. Assist. Tomogr.* **6**: 551–565.
- Rogers, J. G., and Gumplinger, P. (1999). A pixelated 3D Anger camera with light-loss compensation. *IEEE Trans. Nucl. Sci.* **46**: 973–978.
- Saoudi, A., Pepin, C. M., Dion, F., Bentourkia, M., Lecomte, R., Andreaco, M., Casy, M., Nutt, R., and Dautet, H. (1999). Investigation of depth-of-interaction by pulse shape discrimination in multicrystal detectors read out by avalanche photodiodes. *IEEE Trans. Nucl. Sci.* **46**(3): 462–467.
- Schmand, M., Weinhard, K., Casey, M. E., Eriksson, L., *et al.* (1999). Performance evaluation of a new LSO High Resolution Research Tomograph—HRRT. *1999 Conf. Rec. IEEE Nucl. Sci. Symp. Med. Imaging Conf.* M4–2.
- Smith, R., Karp, J. S., Muehllehner, G., Gualtieri, E., and Benard, F. (1997). Singles transmission scans performed post-injection for quantitative whole-body PET imaging. *IEEE Trans. Nucl. Sci.* **44**: 1329–1335.
- Strother, S. C., Casey, M. E., and Hoffman, E. J. (1990). Measuring PET scanner sensitivity: Relating countrates to image signal-to-noise ratios using noise equivalent counts. *IEEE Trans. Nucl. Sci.* **37**: 783–788.
- Ter-Pogossian, M., Mullani, N. A., Hood, J. T., Higgins, C. S., and Ficke, D. C. (1978). Design considerations for a positron emission tomograph (PETT-V) for imaging of brain. *J. Comput. Assist. Tomogr.* **2**: 539–544.
- van Eijk, C. W. E. (2002). Inorganic scintillators in medical imaging. *Phys. Med. Biol.* **47**: R85–R106.
- Vaquero, J. J., Seidel, J., Siegel, S., and Green, M. V. (1998). A depth-encoding PET detector module with improved spatial sampling. *1998 Conf. Rec. IEEE Nucl. Sci. Symp. Med. Imaging Conf.* M6–29.
- Watson, C. C., Eriksson, L., Casey, M. E., *et al.* (2001). Design and performance of collimated coincidence point sources for simultaneous transmission measurements in 3-D PET. *IEEE Trans. Nucl. Sci.* **48**: 673–679.
- Watson, C. C., Newport, D., and Casey, M. E. (1996). A single scatter simulation technique for scatter correction in 3D PET. In “Three-Dimensional Image Reconstruction in Radiology and Nuclear Medicine” (P. Grangeat and J.-L. Amans, eds.), pp. 255–268. Kluwer Academic, Dordrecht.
- Weinhard, K., Schmand, M., Casey, M. E., *et al.* (2002). The ECAT HRRT: Performance and first clinical application of the new high resolution research tomography. *IEEE Trans. Nucl. Sci.* **49**: 104–110.
- Weng, S., and Bettinadi, B. (1993). An automatic segmentation method for fast imaging in PET. *Nucl. Sci. Techniques* **4**(2): 114–119.
- Wong, W. H., Mullani, N. A., *et al.* (1984). Characteristics of small barium fluoride (BaF₂) scintillator for high intrinsic resolution time-of-flight positron emission tomography. *IEEE Trans. Nucl. Sci.* **31**: 381–386.
- Wong, W., Uribe, J., Hicks, K., and Hu, G. (1995). An analog decoding BGO block detector using circular photomultipliers. *IEEE Trans. Nucl. Sci.* **42**: 1095–1101.
- Xu, M., Luk, W. K., *et al.* (1994). Local threshold for segmented attenuation correction of PET imaging of the thorax. *IEEE Trans. Nucl. Sci.* **41**: 1532–1537.